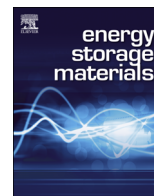




ELSEVIER

Contents lists available at ScienceDirect

## Energy Storage Materials

journal homepage: [www.elsevier.com/locate/ensm](http://www.elsevier.com/locate/ensm)

# Intercalation of cations into partially reduced molybdenum oxide for high-rate pseudocapacitors

Xu Xiao<sup>a,1</sup>, Chuanfang (John) Zhang<sup>b,1</sup>, Shizhe Lin<sup>a</sup>, Liang Huang<sup>a</sup>, Zhimi Hu<sup>a</sup>, Yongliang Cheng<sup>a</sup>, Tianqi Li<sup>a</sup>, Wenming Qiao<sup>b</sup>, Donghui Long<sup>b</sup>, Yunhui Huang<sup>c</sup>, Liqiang Mai<sup>d</sup>, Yury Gogotsi<sup>e</sup>, Jun Zhou<sup>a,\*</sup>

<sup>a</sup> Wuhan National Laboratory for Optoelectronics, School of Optical and Electronic Information, Huazhong University of Science and Technology, Wuhan 430074, PR China

<sup>b</sup> State Key Laboratory of Chemical Engineering, Department of Chemical Engineering, East China University of Science and Technology, Shanghai 200237, PR China

<sup>c</sup> School of Materials Science and Engineering, Huazhong University of Science and Technology, Wuhan 430074, Hubei, PR China

<sup>d</sup> State Key Laboratory of Advanced Technology for Materials Synthesis and Processing, WUT-Harvard Joint Nano Key Laboratory, Wuhan University of Technology, Wuhan 430070, PR China

<sup>e</sup> Department of Materials Science and Engineering, and A.J. Drexel Nanomaterials Institute, Drexel University, Philadelphia, PA 19104, USA

## ARTICLE INFO

## Article history:

Received 27 April 2015

Received in revised form

12 May 2015

Accepted 13 May 2015

Available online 9 June 2015

## Keywords:

MoO<sub>3</sub> nanobelts

Pseudocapacitor

Intercalation

Ion

Energy storage

## ABSTRACT

Intercalation capacitance is emerging as a promising approach to increasing energy density of electrochemical capacitors. However, the number of materials capable of intercalating ions other than small H<sup>+</sup> and Li<sup>+</sup> is limited. Here we report a K<sup>+</sup> preintercalated hydrogenated MoO<sub>3</sub> (K<sub>y</sub>MoO<sub>3-x</sub>) with enhanced conductivity and widened interlayer gaps. Different cations (Mg<sup>2+</sup>, Na<sup>+</sup>, K<sup>+</sup> and Li<sup>+</sup>) were able to intercalate along the (010) facet of K<sub>y</sub>MoO<sub>3-x</sub> with high intercalation capacitance (374 F/cm<sup>3</sup> at 0.5 A/g in 5 M LiCl). The cation intercalation behavior and the origin of the high capacitance have been systematically studied. Using artificial seawater as electrolyte, high volumetric capacitance (188 F/cm<sup>3</sup> at 0.5 A/g) and good rate handling were also achieved. The K<sub>y</sub>MoO<sub>3-x</sub> electrode also showed a similar capacitance (196 F/cm<sup>3</sup> at 0.5 A/g) and cycling performance (89% of initial capacitance maintained after 10,000 cycles) in natural seawater. When K<sub>y</sub>MoO<sub>3-x</sub> was fabricated into a symmetric pseudocapacitor with natural seawater as the electrolyte, the energy density and power density of the electrode reached 0.91 mWh/cm<sup>3</sup> and 6.5 W/cm<sup>3</sup>, respectively. The impressive results indicate K<sub>y</sub>MoO<sub>3-x</sub> is a promising high-power handling pseudocapacitor electrode material.

© 2015 Elsevier B.V. All rights reserved.

## 1. Introduction

Supercapacitors (SCs) have attracted great attention due to their ability of fast charging–discharging, high power density and excellent cycling performance, being able to complement or even substitute batteries in many applications [1–4]. Most of previous research focused on increasing the energy density without compromising the power density [5,6]. Pseudocapacitors have been widely investigated due to their capability to strike the balance between the two parameters [5,6]. The pseudocapacitors may use aqueous, organic and ionic liquid electrolytes [1]. For the sake of

energy density, organic and ionic liquid electrolytes, having a larger voltage window, prevail over the aqueous medium [1]. However, these choices raise environmental concerns. Therefore, abundant, low cost and most of all, environmentally-benign electrolytes would be highly desirable. Aqueous electrolytes, on the other hand, provide high ionic conductivity and fast ion transport kinetics inside the developed pore channels, resulting in high power-handling ability in the pseudocapacitors. Among them, aqueous electrolytes based on lithium, sodium, potassium and magnesium salts are the most common choices. Frackowiak et al. compared these three electrolytes and showed that Li<sub>2</sub>SO<sub>4</sub> could be stable upon a polarization potential close to 2 V, which evoked much research interest toward choosing green, cheap and sustainable aqueous electrolytes [7].

\* Corresponding author.

E-mail address: [jun.zhou@mail.hust.edu.cn](mailto:jun.zhou@mail.hust.edu.cn) (J. Zhou).<sup>1</sup> Authors contributed equally.

Recently, a new kind of pseudocapacitance called intercalation-induced pseudocapacitance has been demonstrated in layered or tunneled materials [8]. Dunn et al. pointed out the high-rate performance when  $\text{Li}^+$  ions were inserted into mesoporous and nanocrystalline films of orthorhombic  $\text{Nb}_2\text{O}_5$  [8b–d]. During the repeated charging–discharging, phase change is absent upon the ion intercalation, and therefore the bulk active sites could be further utilized, rendering high volumetric capacitance [8e]. Similar to the structure of  $\text{Nb}_2\text{O}_5$ , orthorhombic  $\text{MoO}_3$  ( $\alpha\text{-MoO}_3$ ) is the most thermodynamically stable phase among three polymorphs (orthorhombic, monoclinic and hexagonal), which consists of two-dimensional layers of  $\text{MoO}_6$  octahedra bonded by van der Waals bonds [8b]. Such a structure with interlayer gaps is highly favorable for the  $\text{Li}^+$  insertion/extraction with up to 1.5  $\text{Li}/\text{Mo}$  [9]. The multiple valences of  $\alpha\text{-MoO}_3$  suggest the possibility of electron transfer reactions that deliver a higher capacitance compared to carbon materials. Unfortunately, this kind of pseudocapacitance is confined to the surface/near surface redox reaction with insufficient utilization of the bulk active sites. Therefore, extensive studies were focused on designing the nano/micro architecture to enhance the electrochemical performance of  $\text{MoO}_3$ . Our previous work reported a core–shell  $\text{WO}_{3-x}/\text{MoO}_{3-x}$  composite which showed  $500 \text{ mF}/\text{cm}^2$  at  $1 \text{ mA}/\text{cm}^2$  [10]. Coleman et al. reported on the  $\text{MoO}_3$  sheet/CNT hybrid electrode with  $540 \text{ F}/\text{g}$  at  $0.1 \text{ mV}/\text{s}$  [11]. However, the poor conductivity of  $\text{MoO}_3$  greatly hinders the electron transport and limits the capacitance and rate performance [12]. Moreover, poor conductivity could cause the uneven distribution of voltage in some active sites during charge/discharge process, leading to hyperpolarization and structure damage [13,14]. As a result,  $\text{MoO}_3$  usually has rapid degradation and poor cycling performance. Some reports resorted to the cation (such as  $\text{H}^+$  and  $\text{Li}^+$ ) insertion to promote the electric conductivity of  $\text{MoO}_3$  [15]. Nevertheless, excess of inserted cations may distort and even destroy the layered structure [15b–d]. Therefore, increasing the electronic conductivity while preserving the structure with large interlayer spaces in  $\text{MoO}_3$  is necessary for achieving fast ion intercalation in aqueous electrolytes.

Herein, we report on a new  $\text{MoO}_3$  derivative –  $\text{K}^+$  inserted hydrogenated  $\text{MoO}_3$  ( $\text{K}_y\text{MoO}_{3-x}$ ). Oxygen vacancies were firstly introduced into  $\text{MoO}_3$  nanobelts by hydrogenation, and the resulting  $\text{MoO}_{3-\delta}$  was further reacted with  $\text{KBH}_4$ , leading to widened interlayer distance and enhanced conductivity compared to  $\text{MoO}_3$ . Cations ( $\text{Li}^+$ ,  $\text{Mg}^{2+}$ ,  $\text{Na}^+$  and  $\text{K}^+$ ) with different ion dimensions were capable to intercalate into the interlayers and their intercalation kinetics were analyzed systematically.  $\text{K}_y\text{MoO}_{3-x}$  has demonstrated high volumetric capacitance and excellent cycling performance in artificial and natural seawater electrolytes.

## 2. Experimental

### 2.1. Synthesis of $\text{K}_y\text{MoO}_{3-x}$

$\text{MoO}_3$  nanobelts were produced using hydrothermal synthesis. Typically, 2 g of molybdenum powder (Aladdin, 99.5%) was added to 10 mL deionized water and stirred to achieve a uniform mixture. Then, 20 mL  $\text{H}_2\text{O}_2$  was slowly added. After stirring for 30 min, the solution was transferred to a Teflon-lined stainless steel autoclave and heated at  $180^\circ\text{C}$  for 12 h. The precipitate was filtered and rinsed with deionized water, followed by drying at  $70^\circ\text{C}$  for 12 h. Then the  $\text{MoO}_3$  was hydrogenated in  $\text{H}_2/\text{Ar}$  (10 vol%  $\text{H}_2$ ) at  $350^\circ\text{C}$  for 5 h to obtain  $\text{MoO}_{3-\delta}$ . 500 mg  $\text{MoO}_{3-\delta}$  was dispersed in 50 mL ethanol and let to react with 0.065 g  $\text{KBH}_4$  for 10 h under stirring. Finally, the as-fabricated  $\text{K}_y\text{MoO}_{3-x}$  was filtered, washed several times, and dried at  $70^\circ\text{C}$  for 12 h.

### 2.2. Preparation of freestanding films

The vacuum filtration method was used to fabricate the freestanding films. 0.4 g SDS was firstly dissolved in 50 mL deionized water, which contains 0.021 g CNTs (Blue Nano, China) and 0.039 g  $\text{K}_y\text{MoO}_{3-x}$ . After 20 min sonication, the as-obtained solution was filtered through a cellulose membrane (220 nm pore size). The obtained filter cake was dried at  $70^\circ\text{C}$  for 4 min and then peeled off to obtain a freestanding film with thickness of 20  $\mu\text{m}$ . Electrodes were obtained after punching the film to produce 5 mm in diameter disks. The density of each electrode was  $0.9\text{--}0.98 \text{ g}/\text{cm}^3$  ( $1.8\text{--}1.96 \text{ mg}/\text{cm}^2$ ).

### 2.3. Preparation of the artificial electrolyte

To prepare the artificial seawater electrolyte, 26.726 g NaCl, 2.26 g  $\text{MgCl}_2$ , 3.248 g  $\text{MgSO}_4$ , 1.153 g  $\text{CaCl}_2$ , 0.198 g  $\text{NaHCO}_3$ , 0.721 g KCl and 0.058 g NaBr were dissolved in 1 L deionized water.

### 2.4. Characterization

The morphology and structure of the samples were studied by field-emission scanning electron microscopy (FE-SEM, FEI Nova 450 Nano), high-resolution transmission electron microscopy (HRTEM, TECNAI), X-ray diffraction (XRD, X'Pert Pro, PANanalytical) and X-ray photoelectron spectroscopy (XPS, ESCALab250). Resistance measurements were conducted by the four-point probe method (RTS-8, China). All of the electrochemical tests were carried out using Autolab PGSTAT302N and CHI660E. For the typical three-electrode setup, Ag/AgCl (CHI, USA) was the reference electrode, YP-50 (Kuraray Chemical, Japan) was the counter electrode, and a Celgard separator was used (Celgard, USA). A symmetric device was constructed based on  $\text{K}_y\text{MoO}_{3-x}$  electrodes with natural seawater as electrolyte. The voltage range was  $0\text{--}0.65 \text{ V}$ . All the tests were conducted in Swagelok cells (Swagelok, USA). Electrochemical impedance was measured from 10 MHz to 1 MHz with a potential amplitude of 10 mV. For natural seawater measurements, the seawater (directly collected from sea around Shenzhen, China) was firstly filtered to eliminate microbial impurities.

## 3. Results and discussion

The fabrication process is schematically shown in Fig. 1a. Firstly, greyish  $\text{MoO}_3$  was synthesized hydrothermally by using Mo powder and  $\text{H}_2\text{O}_2$  [15a]. The obtained  $\text{MoO}_3$  was hydrogenated [16,17] and formed the light-blue  $\text{MoO}_{3-\delta}$  (Fig. S1a), which was further reacted with  $\text{KBH}_4$  in ethanol, producing the dark-purple  $\text{K}_y\text{MoO}_{3-x}$  [15e]. Fig. 1b indicates the nanobelt structure of  $\text{K}_y\text{MoO}_{3-x}$  with 3–5  $\mu\text{m}$  in length and  $\sim 180 \text{ nm}$  in width, Figs. S1b and S2a show further SEM and TEM images. High-resolution TEM image and the corresponding selected area electron diffraction (SAED) pattern (Fig. S2b) reveal that the  $\text{K}_y\text{MoO}_{3-x}$  nanobelts are single-crystalline and grow along (010) plane.

Local energy dispersive X-ray spectroscopy (EDS) analysis of the  $\text{K}_y\text{MoO}_{3-x}$  nanobelts (Fig. S2c) detected Mo, O and K signals, in addition to Cu and C signals from the TEM grid. Moreover, the element mapping of the rectangular area in Fig. 1c suggests that these three elements are distributed uniformly in  $\text{K}_y\text{MoO}_{3-x}$  (Fig. 1c–f), showing that  $\text{K}^+$  ions have been successfully inserted into the nanocrystalline structure of  $\text{MoO}_3$ . The K content is determined to be  $\sim 1.22 \text{ wt}\%$  by inductively coupled plasma optical emission spectroscopy (ICP-OES). As expected,  $\text{K}_y\text{MoO}_{3-x}$  exhibited an enhanced  $\text{Mo}^{4+}$  valence state compared to the as-

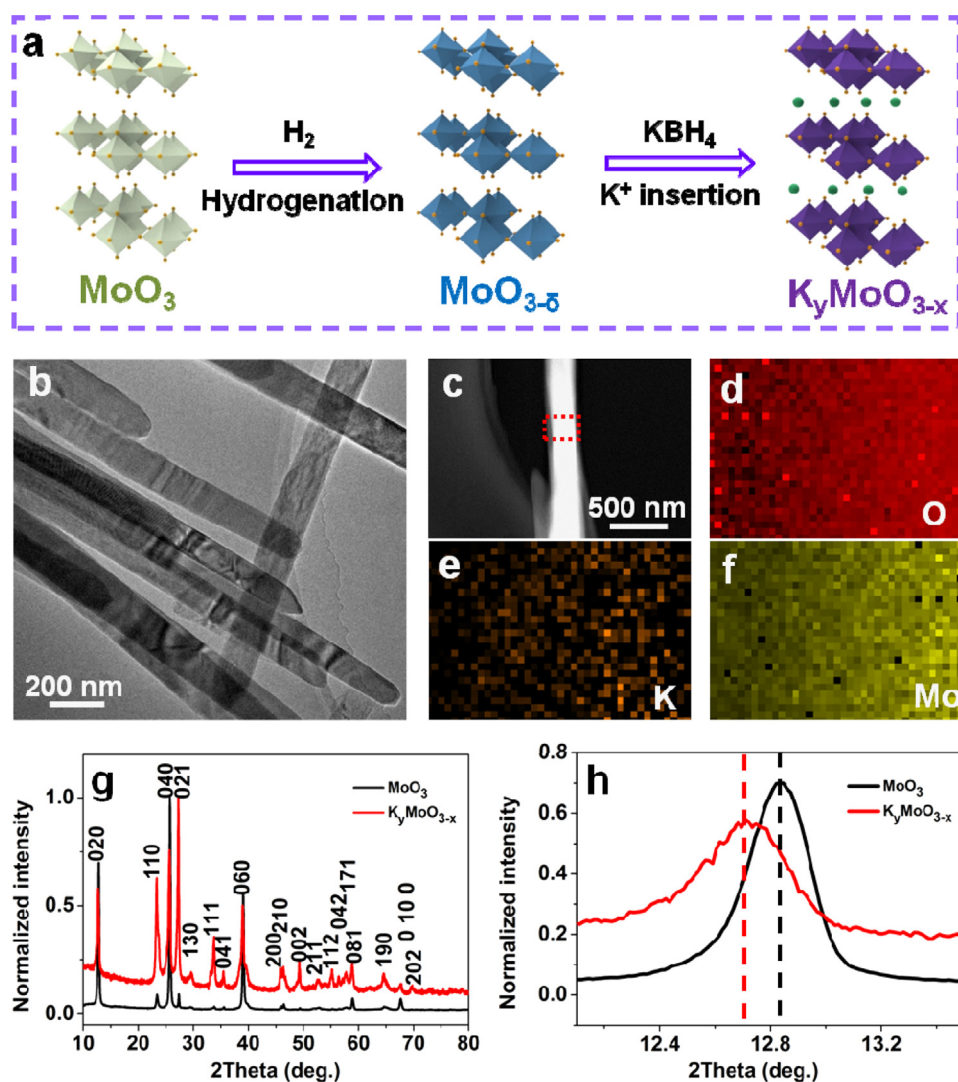


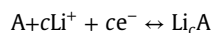
**Fig. 1.** (a) Fabrication schematic of  $K_y\text{MoO}_{3-x}$ . (b) Low-resolution TEM image of  $K_y\text{MoO}_{3-x}$  nanobelts with the width of  $\sim 180$  nm. (c)–(f) EDS mapping in TEM, indicating that Mo, O and K are distributed uniformly in  $K_y\text{MoO}_{3-x}$ . (g) and (h) XRD patterns of  $K_y\text{MoO}_{3-x}$  and  $\text{MoO}_3$ , (020) diffraction peaks of  $K_y\text{MoO}_{3-x}$  nanobelts are shifted to lower angles due to increased lattice spacing.

prepared  $\text{MoO}_3$ , which was verified by the X-ray photoelectron spectroscopy (XPS) results (Fig. S3). No  $\text{Mo}^{5+}$  was found in the  $K_y\text{MoO}_{3-x}$  indicated that  $\text{Mo}^{6+}$  was directly reduced to  $\text{Mo}^{4+}$  after hydrogenation at low temperatures (less than  $450^\circ\text{C}$ ) [18].

The structure of  $K_y\text{MoO}_{3-x}$  nanobelts was characterized by X-ray diffraction (XRD), as shown in Fig. 1g. All of the diffraction peaks can be indexed as orthorhombic  $\alpha\text{-MoO}_3$  (JCPDS reference card no. 05-0508). Compared to that of  $\text{MoO}_3$  nanobelts, (010) diffraction peaks of  $K_y\text{MoO}_{3-x}$  nanobelts detectably shifted to lower angles (Fig. 1h), due to expansion along [010] direction. Since no detectable change is found along [100] and [001] directions (Fig. S4), the enlarged interlayer spacing implies that the inserted  $\text{K}^+$  is located at (010) planes of  $\text{MoO}_{3-\delta}$ .

The resistance of  $K_y\text{MoO}_{3-x}$  measured by the four-point probe method (Table S1) is two orders of magnitude lower compared to  $\text{MoO}_3$ . To further confirm the effects of improved electronic conductivity and widened interlayer gaps on the electrochemical performance, electrochemical tests were conducted in 5 M LiCl in three-electrode setup. As discussed in our previous work, [19a] the freestanding film architecture is advantageous, thanks to elimination of binder, easier fabrication, improved volume/mass

utilization and overall performance. Herein, freestanding  $K_y\text{MoO}_{3-x}/\text{CNT}$  (65/35 wt%, called “ $K_y\text{MoO}_{3-x}$  electrode” thereafter) film (Fig. S5) was fabricated [19a]. The cyclic voltammetry (CV) curve of  $K_y\text{MoO}_{3-x}$  electrode shows a larger area and an extra pair of redox peaks compared to  $\text{MoO}_3$  (Figs. 2a and S6a), suggesting a higher pseudocapacitance contribution in the former. Such a pseudocapacitance definitely stemmed from  $\text{Li}^+$  intercalation–redox reaction process (existence of broad peaks in Fig. 2a), similar to ion intercalation in  $\text{Ti}_3\text{C}_2\text{T}_x$  MXene [20a]. The electrochemical reaction in LiCl during  $\text{Li}^+$  intercalation could be written as following:



where A is  $K_y\text{MoO}_{3-x}$  or  $\text{MoO}_3$ , and c is the number of inserted ions. For  $K_y\text{MoO}_{3-x}$ , the cathodic peak ( $-0.65$  V vs Ag/AgCl) and anodic peak ( $-0.45$  V vs Ag/AgCl) correspond to the  $\text{Li}_c\text{K}_y\text{MoO}_{3-x}$  formation and delithiation back to  $K_y\text{MoO}_{3-x}$ , respectively. To further unveil the diffusion kinetics, CVs at various sweep rates were recorded and diffusion limitations were analyzed. As shown in Fig. 2b, the redox peaks are maintained up to 100 mV/s without apparent potential shift, indicating that the  $\text{Li}^+$  intercalation into  $K_y\text{MoO}_{3-x}$  is pseudocapacitive (surface controlled) rather than

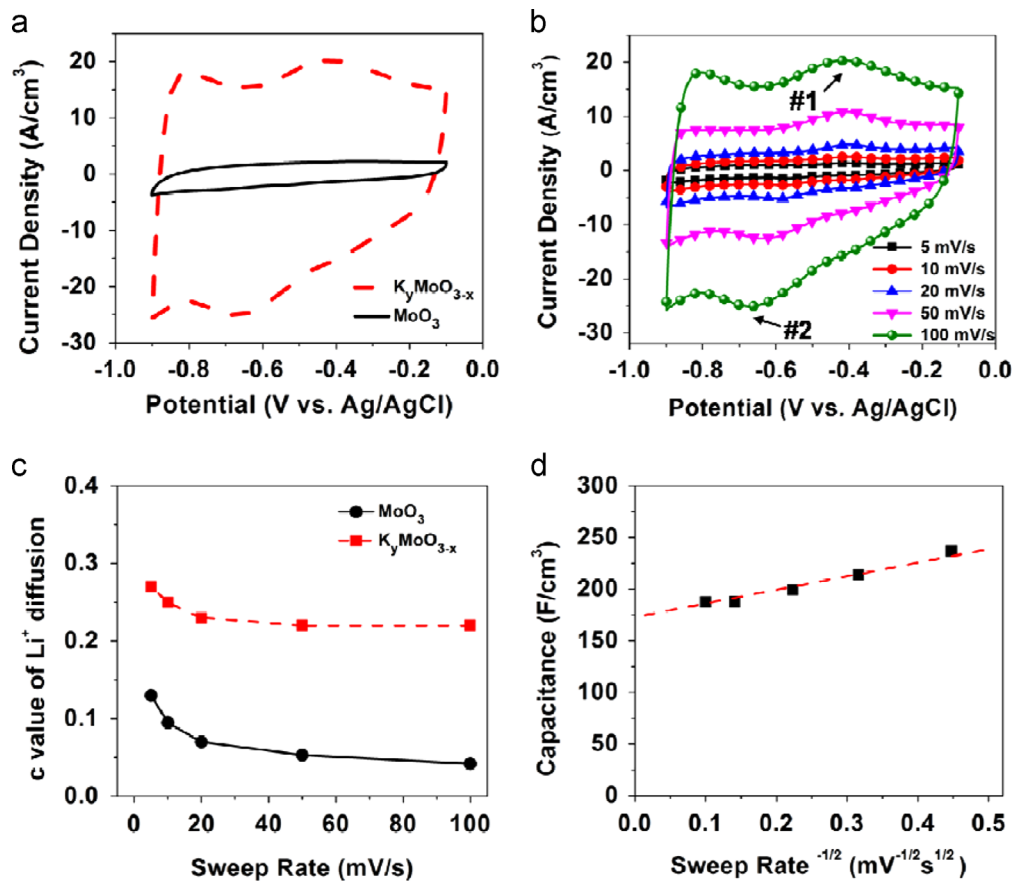


**Fig. 2.** (a) CV curves of  $K_yMoO_{3-x}$  and  $MoO_3$  at 100 mV/s in 5 M LiCl. (b) CV curves of  $K_yMoO_{3-x}$  from 5 mV/s to 100 mV/s. (c) Numbers of  $Li^+$  ions inserted in the tunneled  $MoO_3$  and  $K_yMoO_{3-x}$  (c value of  $Li^+$  diffusion). (d) Capacitance as a function of sweep rate<sup>-1/2</sup> plot used to determine the infinite sweep rate capacitance. The capacitance is calculated from equation:  $\int(I)/(\nu\Delta V)$  from the CV curves.

solid-state diffusion controlled (battery-like). Similar  $Li^+$  intercalation behavior could also be found in the T-Nb<sub>2</sub>O<sub>5</sub> [8b] and mesoporous TiO<sub>2</sub>-B microspheres [20b–c]. We also calculated the number of inserted  $Li^+$  in  $K_yMoO_{3-x}$  and  $MoO_3$  (c value) as shown in Fig. 2c (see Supporting information for calculation details). At 5 mV/s (discharge time 160 s), 0.27  $Li^+$  could be inserted into  $K_yMoO_{3-x}$  while only 0.13  $Li^+$  into  $MoO_3$ . When the sweep rate increased to 100 mV/s, the number of inserted  $Li^+$  in  $K_yMoO_{3-x}$  remained almost constant (change from 0.27 to 0.22), however only 0.042  $Li^+$  inserted into  $MoO_3$ . This phenomenon demonstrates that due to enlarged interlayer distance, more  $Li^+$  ions intercalated into  $K_yMoO_{3-x}$  than  $MoO_3$ , especially at high sweep rates. In general, the capacitance can be divided into surface-controlled and diffusion-controlled components [8c,19b]. Assuming the diffusion-controlled capacitance is a semi-infinite linear diffusion process, which has a function of  $\nu^{-1/2}$ , the intercept of Y axis of Fig. 2d could be deemed as surface-controlled capacitance (the sweep rate approaches infinite), which reaches 173 F/cm<sup>3</sup> in  $K_yMoO_{3-x}$ . The sweep rates would change the ratio of these two capacitance sources. For example, at 5 mV/s (discharge time ~160 s), the diffusion-controlled capacitance reaches 57 F/cm<sup>3</sup>, accounting for < 27% in the total capacitance. For the sweep rate > 5 mV/s, the percentage of diffusion-controlled capacitance decreases gradually and at 100 mV/s the capacitance is almost completely derived from surface processes (Fig. 2d).

Galvanostatic charge–discharge (GCD) curves of  $K_yMoO_{3-x}$  (Fig. 3a), are symmetric and show only a small IR drop at a high current density of 100 A/g. Excellent power handling capability is the key property of electrochemical capacitors. Fig. 3b shows the

volumetric/gravimetric capacitances of the two samples (see Supporting information for calculation details). The volumetric capacitance reaches 306 F/cm<sup>3</sup> (325 F/g) at 0.5 A/g, much larger than for pure  $MoO_3$  (122 F/cm<sup>3</sup>), porous carbons (< 180 F/cm<sup>3</sup>) [21] and comparable with layered Ti<sub>3</sub>C<sub>2</sub>T<sub>x</sub> MXene in neutral aqueous electrolyte (~330 F/cm<sup>3</sup>) [20a], and there are very few reports on a higher volumetric capacitance [8]. As shown in Fig. 3b, the capacitance decreases from 0.5 A/g to 5 A/g and then becomes quite stable from 5 to 100 A/g. This phenomenon could be related to the capacitance origin under different current densities. For the diffusion-controlled process, more ions could intercalate to the interlayer gaps at low current density, resulting in a higher capacitance compared to  $MoO_3$ . This process becomes more obvious when elevating the current density from 0.5 A/g to 5 A/g, leading to incomplete electron and mass transfer and thus lowering the capacitance. When current density rises above 5 A/g, the process enters the surface-controlled regime. At such a high current density (short charge–discharge time), ions adsorb on the accessible surfaces instead of penetrating the interior of  $K_yMoO_{3-x}$ . In this case, an enhanced conductivity of the material is desired, similar to carbon onions or other highly conductive electrode materials [22,23]. The pseudocapacitance of  $K_yMoO_{3-x}$  reached 175 F/cm<sup>3</sup> at 100 A/g under a high mass loading (1.8 mg/cm<sup>2</sup>), which is in excellent agreement with surface-controlled capacitance (173 F/cm<sup>3</sup>) in Fig. 2d. On the contrary,  $MoO_3$  shows poor capacitance and fast capacitance decay when current density rises to 100 A/g, suggesting the crucial effects of conductivity and interlayer spacing on the capacitance and rate response. The enhanced conductivity could also be seen from the

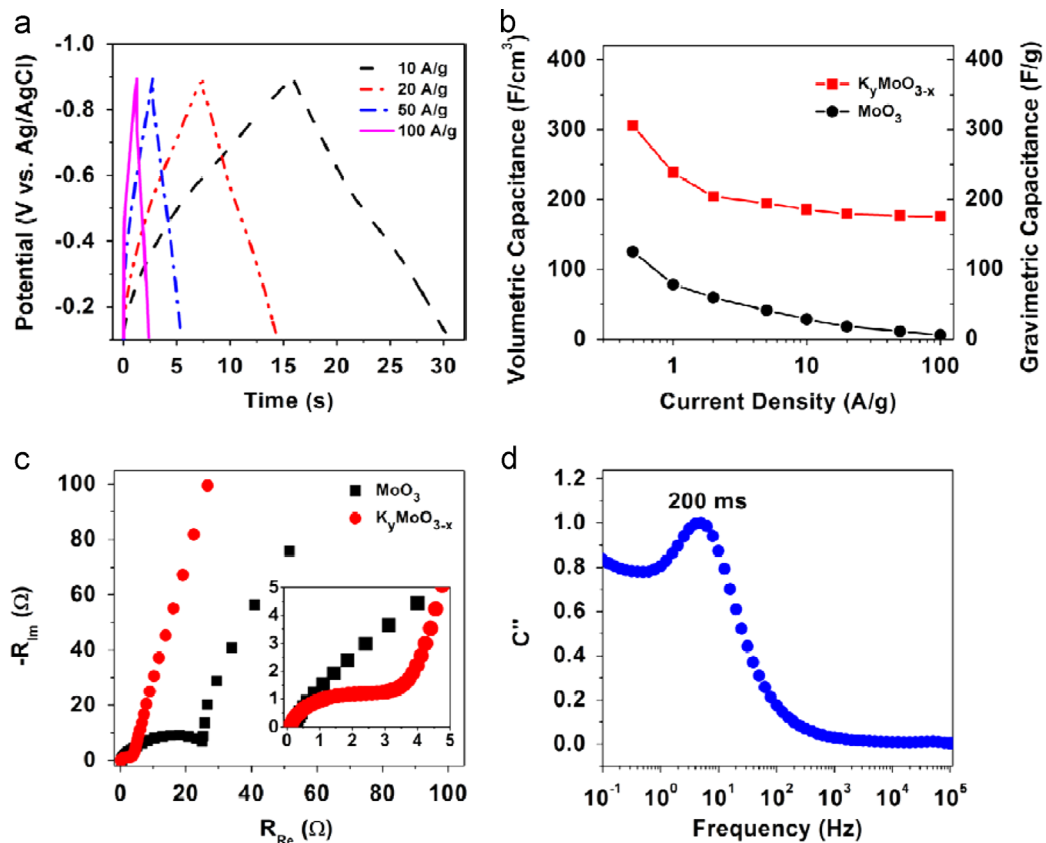


**Fig. 3.** (a) GCD curves of  $K_yMoO_{3-x}$  from 10 to 100 A/g in LiCl. The quasi-linear shape indicates pseudocapacitive behavior. Besides, the symmetric charge and discharge branches suggest high coulombic efficiency. (b) Volumetric and gravimetric capacitance vs current density for  $K_yMoO_{3-x}$  and  $MoO_3$ . (c) Nyquist plots for  $K_yMoO_{3-x}$  and  $MoO_3$ . (d) Normalized  $C''$  for  $K_yMoO_{3-x}$ .  $C'' = Z'/2\pi f|Z|^2$ , where  $Z'$  is the real part of  $Z$ ,  $f$  is the frequency, all of the data was obtained from EIS measurement.

electrochemical impedance spectroscopy (EIS) data in Fig. 3c, as a smaller semicircle in  $K_yMoO_{3-x}$  compared to  $MoO_3$ . Fig. 3d shows the imaginary capacitance vs frequency. The knee frequency ( $f_0$ ) is  $\sim 5$  Hz, indicating the time constant ( $\tau_0$ ) of  $\sim 200$  ms according to the equation  $\tau_0 = 1/f_0$ , which much better than commercial activated carbons [23,24]. This high power handling ability explains well the stable capacitance up to 100 A/g (Fig. 3b).

Besides  $Li^+$ , the widened interlayer spacing in  $K_yMoO_{3-x}$  also embraces larger cations for intercalation. CV curves (Fig. 4a) and GCD profiles (Fig. 4b) of  $K_yMoO_{3-x}$  tested in NaCl, KCl and  $MgSO_4$  electrolytes are presented. The different peak shapes and positions in Fig. 4a indicate different cation-intercalation processes. To further understand the effects of cation dimension on the ion diffusion/intercalation process, we also calculated the  $c$  value for  $Na^+$ ,  $K^+$  and  $Mg^{2+}$  ions in  $K_yMoO_{3-x}$  (Fig. 4c). At 5 mV/s, 0.21  $Na^+$  could be inserted into  $K_yMoO_{3-x}$  while only 0.14 for  $K^+$ , which could explain the higher capacitance in NaCl than KCl, as shown in Fig. 4d. Only 0.09  $K^+$  could intercalate  $K_yMoO_{3-x}$  at 100 mV/s, which also confirms our hypothesis that less  $K^+$  participated in the charge storage at high rates (Fig. 4d) due to its larger ion size compared to  $Na^+$ . For  $Mg^{2+}$ , the inserted ions number is 0.12 at 5 mV/s. However, considering it is divalent, intercalation of 0.12  $Mg^{2+}$  equivalently transfer  $0.24e^-$ , resulting in a higher capacitance in  $Mg^{2+}$  than  $Na^+$  containing electrolyte. The diffusion kinetics was also analyzed and presented in Fig. S6. Fig. 4d also summarizes the rate performances of  $K_yMoO_{3-x}$  in these three electrolytes. Notably,  $Mg^{2+}$  has the highest capacitance of 265 F/cm<sup>3</sup> at 0.5 A/g while  $Na^+$  has the best capacitance retention-high rates (70% retention from 0.5 A/g to 50 A/g). This could be interpreted as similar ion size of  $Mg^{2+}$  and  $Li^+$  (Table S2). For  $Na^+$ ,

owing to its larger ion size than  $Li^+$ , even at a low current density, relatively fewer ions could be intercalated, translating to a volumetric capacitance of 183 F/cm<sup>3</sup>. For  $K^+$ , a capacitance of 180 F/cm<sup>3</sup> was reached at 0.5 A/g. However, due to its much larger ion size compared to  $Na^+$ , less  $K^+$  participated in the diffusion/intercalation process, leading to a lower capacitance when increasing the current density. Even so, this value is still encouraging because few papers reported high intercalation capacitance in electrolytes with cation size larger than  $Li^+$  [8c].

Choosing a cheap and environmentally benign electrolyte would be the first step towards building green and economic pseudocapacitors [25]. Since  $K_yMoO_{3-x}$  performed well in  $Na^+$ ,  $K^+$  and  $Mg^{2+}$ -containing chloride and sulfate electrolytes, one can easily choose seawater as a possible electrolyte. The schematic of the seawater-electrolyte device is shown in Fig. 5a. The advantage is that if supercapacitors are used to store energy from solar panels or wind power generators that power capacitive water desalination units, radios or other emergency equipments on lifeboats, they can be stored for years without electrolyte, avoiding degradation, and filled with seawater when needed. Corrosion of stainless steel current collectors, which may occur in seawater, is also not an issue in this relatively short-term application. A series of electrochemical tests, such as CV (Fig. 5b) and GCD (Fig. 5c) were conducted in seawater. Multiple peaks can be seen in CV curves, corresponding to intercalation of  $Na^+$ ,  $K^+$  and  $Mg^{2+}$  ions into  $K_yMoO_{3-x}$ . The quasi-linear shape of GCD curves with a small IR drop even at 20 A/g (Fig. 5c) suggests facile ion/electrons transport and good rate performance. A high volumetric capacitance (196 F/cm<sup>3</sup>) was reached with almost 50% retention at 20 A/g (Fig. 5d). After 10,000 GCD cycles in the natural seawater,

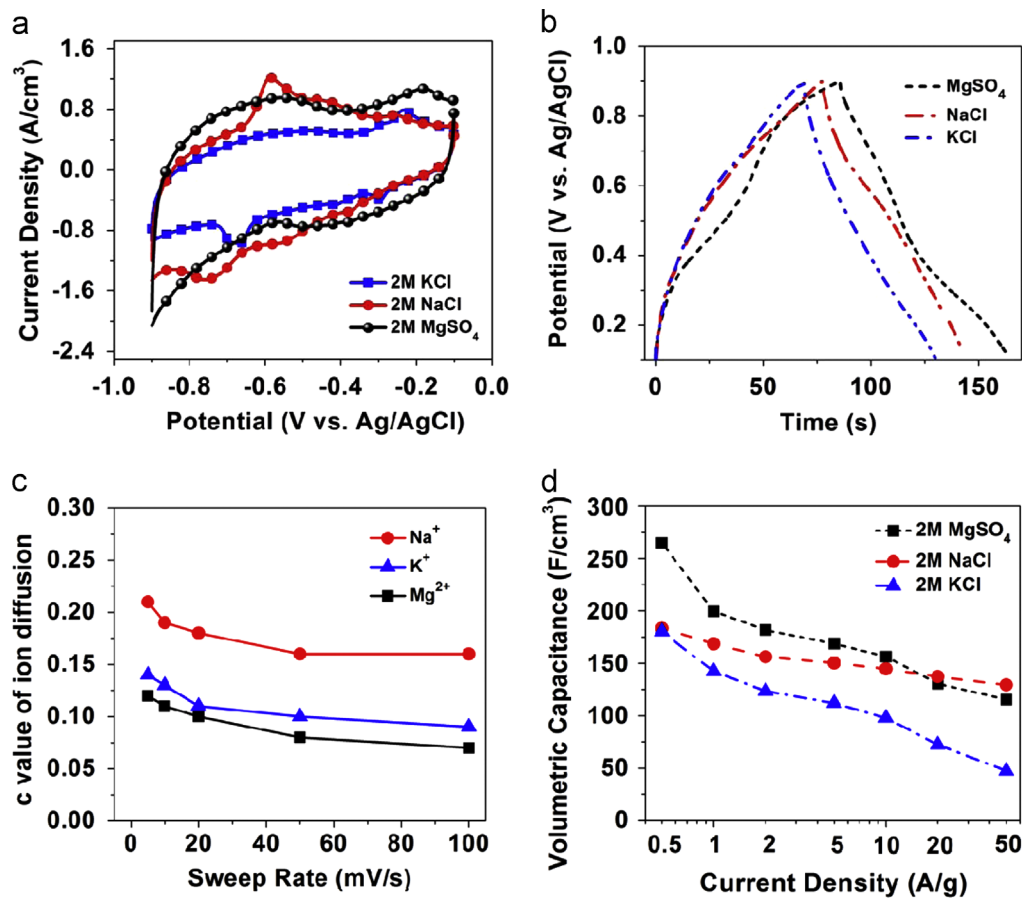


**Fig. 4.** (a) CV curves of  $K_yMoO_{3-x}$  in KCl, NaCl and  $MgSO_4$  at 5 mV/s. The different peak shapes and positions indicate different cation intercalation processes. (b) GCD curves of  $K_yMoO_{3-x}$  in different electrolytes at 2 A/g. Bends/shoulders could be seen in each electrolyte, corresponding to the redox processes that give broad peaks in the CV curves. (c) Effect of cation size on the c value in  $K_yMoO_{3-x}$ . (d) Volumetric capacitance vs current density for  $K_yMoO_{3-x}$  in different electrolytes. The capacitance is calculated based on charge/discharge profiles.

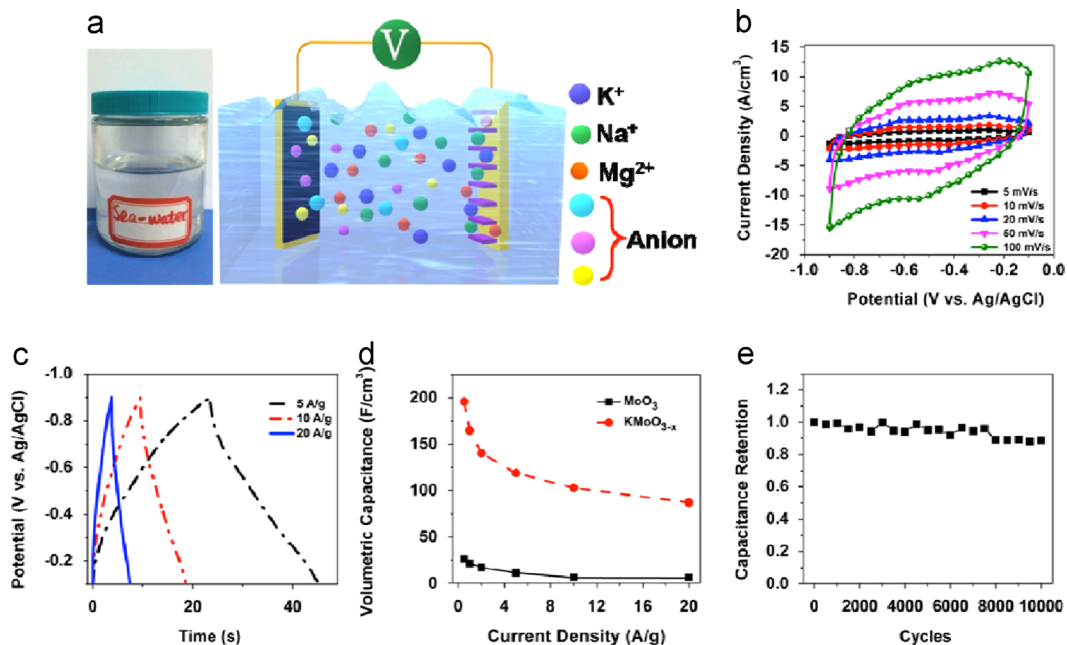


**Fig. 5.** (a) Schematic of green pseudocapacitor using seawater as electrolyte. (b) CV curves of  $K_yMoO_{3-x}$  in seawater from 5 to 100 mV/s. (c) GCD curves of  $K_yMoO_{3-x}$  in seawater from 5 to 20 A/g. (d) Volumetric capacitance vs current density for  $K_yMoO_{3-x}$  and  $MoO_3$  in seawater. (e) Cycling stability of  $K_yMoO_{3-x}$  in seawater tested at a current density of 1 A/g. (For interpretation of the references to color in this figure legend, the reader is referred to the web version of this article.)

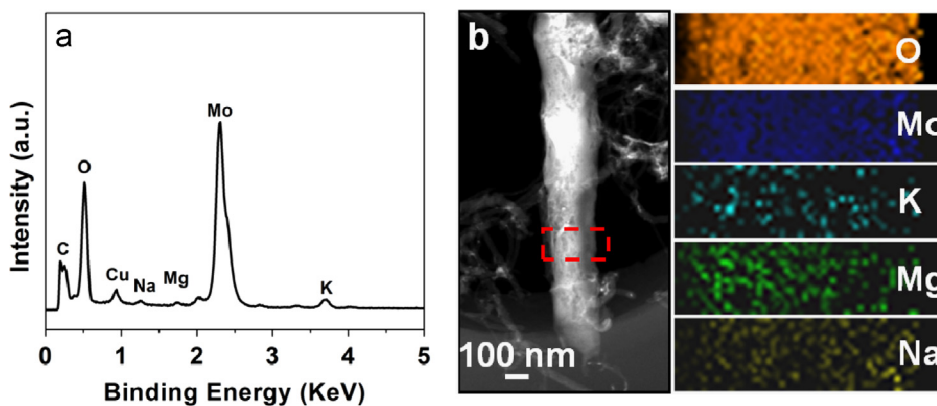


**Fig. 6.** (a) EDS spectrum. (b) EDS elemental maps from TEM. Na, K and Mg signals are detected, but not Cl, suggesting the cation intercalation rather than salt adsorption occurred during the cyclic charge–discharge.

$K_yMoO_{3-x}$  still kept 89% of initial capacitance, much better than  $MoO_3$  in 0.1 M TBAP (45% after 800 cycles) [26] and  $MoO_3/ZnO$  in 1 M  $Na_2SO_4$  (89.7% after 1000 cycles) [27]. Moreover, these results were achieved under a mass loading of 1.8 mg/cm<sup>2</sup>, larger than the typically reported loadings for pseudocapacitors in literature, making the  $K_yMoO_{3-x}$  even more attractive [6]. We assume that the good conductivity of  $K_yMoO_{3-x}$  allows an even potential distribution across the electrode, and prevents hyperpolarization and rapid structure degradation during repeated charge–discharge. This could be confirmed from the Fig. S8, as no obvious change is observed in SEM image of the electrode before and after 1000 charge/discharge cycles. It should be noted that the concentration of cations in the seawater varies in different spots of sea and there are also organic substances in the sea, which may influence the electrochemical performance, leading to redox peaks in CVs obtained using natural seawater. To confirm that the results of our study were not affected by random factors, artificial seawater was prepared (details in Table S3). Since the electrochemical performance was almost same in both natural and artificial seawater, as shown in Fig. S9, one can confidently draw the conclusion that the natural seawater is suitable as electrolyte candidate for  $K_yMoO_{3-x}$ .

After the cation-insertion process in seawater, the  $K_yMoO_{3-x}$  electrode was washed in deionized water several times to eliminate the physisorbed ions. Then EDS measurements were further conducted to verify that the cations' intercalation instead of physical salt adsorption took place on the electrode. As shown in Fig. 6a, Na, K and Mg signals are detected, but not Cl. Moreover, they are distributed uniformly, as shown in Fig. 6b, demonstrating intercalation of cations during charging.

Furthermore, a two-electrode symmetric pseudocapacitor cell was assembled and tested in seawater to reveal the device performance of  $K_yMoO_{3-x}$ . The quasi-rectangular CV shape of  $K_yMoO_{3-x}$  at all scan rates (Fig. S11a) indicates the capacitive intercalation behavior with rapid current responses. Notably, the cell shows energy density of 0.91 mWh/cm<sup>3</sup> with power density of 6.5 W/cm<sup>3</sup> (Fig. S11b), which is comparable to d-Ti<sub>3</sub>C<sub>2</sub> in  $K_2SO_4$  and graphene in aqueous electrolyte [20a,28]. Moreover, the power density is larger than our previous reports on asymmetric SCs [10,13]. Good capacitance of  $K_yMoO_{3-x}$  in seawater suggests that this material can also be used in water desalination units, where only carbons are currently used [25,29].

#### 4. Conclusion

In summary, the  $MoO_3$  derivative –  $K_yMoO_{3-x}$  – was prepared using hydrogenation and  $K^+$  insertion. The  $K_yMoO_{3-x}$  showed

enhanced electric conductivity and enlarged interlayer spacing, resulting in high volumetric capacitance (305 F/cm<sup>3</sup> at 0.5 A/g) and excellent rate performance (175 F/cm<sup>3</sup> at 100 A/g) in LiCl electrolyte. Different cations ( $Na^+$ ,  $K^+$ , and  $Mg^{2+}$ ) were capable to intercalate along (010) plane and showed a good electrochemical performance in aqueous electrolytes, including natural and artificial seawater. It turned out that intercalation is a highly reversible pseudocapacitive process. Using natural seawater as the electrolyte,  $K_yMoO_{3-x}$  demonstrates 185 F/cm<sup>3</sup> at 0.5 A/g and excellent cycling performance (89% of initial capacitance after 10,000 cycles). Such an enhanced performance compared to  $MoO_3$  could be attributed to the critical hydrogenation and  $K^+$  inserted treatments with enhanced electrical and ionic conductivity. We believe that the presented strategy is applicable to other layered or tunneled materials for enhancing their electrical conductivity and increasing interlayer gaps for applications in energy storage, desalination, photocatalysis, electrochromic devices, gas sensing, etc.

#### Acknowledgment

This work was financially supported by the National Natural Science Foundation of China (51322210, 61434001) and Director Fund of WNLO. The authors thank Mr. Z. H. Peng, Mr. J. Y. Sun, and Dr. J. Su for the help in experiments, and Dr. Z. F. Li and Prof. Y. H. Zhou for their help in resistance measurement. The authors also acknowledge support of the Analysis and Testing Center of Huazhong University of Science and Technology.

#### Appendix A. Supplementary material

Supplementary data associated with this article can be found in the online version at <http://dx.doi.org/10.1016/j.ensm.2015.05.001>.

#### References

- [1] P. Simon, Y. Gogotsi, *Nat. Mater.* 7 (2008) 845–854.
- [2] J. Ren, W. Bai, G. Guan, Y. Zhang, H. Peng, *Adv. Mater.* 25 (2013) 5965–5970.
- [3] L.Q. Mai, A. Minhas-Khan, X. Tian, K.M. Hercule, Y.L. Zhao, X. Lin, X. Xu, *Nat. Commun.* 4 (2013) 2923–2929.
- [4] P. Simon, Y. Gogotsi, B. Dunn, *Science* 343 (2014) 1210–1211.
- [5] J.R. Miller, A.F. Burke, *Electrochem. Soc. Interface* 17 (2008) 53–57.
- [6] V. Augustyn, P. Simon, B. Dunn, *Energy Environ. Sci.* 7 (2014) 1597–1614.
- [7] F. Beguin, Q. Gao, E. Raymundo-Pinero, L. Demarconnay, *Energy Environ. Sci.* 5 (2012) 9611–9618.

- [8] (a) J. Wang, J. Polleux, J. Lim, B. Dunn, *J. Phys. Chem. C* 111 (2007) 14925–14931;  
(b) V. Augustyn, J. Come, M.A. Lowe, J.W. Kim, P.L. Taberna, S.H. Tolbert, H. D. Abruna, P. Simon, B. Dunn, *Nat. Mater.* 12 (2013) 518–522;  
(c) J.W. Kim, V. Augustyn, B. Dunn, *Adv. Energy Mater.* 2 (2012) 141–148;  
(d) C. Zhang, R. Maloney, M.R. Lukatskaya, M. Beidaghi, B. Dyatkin, E. Perre, D. Long, W. Qiao, B. Dunn, Y. Gogotsi, *J. Power Sources* 274 (2015) 121–129;  
(e) T. Brezesinski, J. Wang, S.H. Tolbert, B. Dunn, *Nat. Mater.* 9 (2010) 146–151.
- [9] T. Tsumura, M. Inagaki, *Solid State Ion.* 104 (1997) 183–189.
- [10] X. Xiao, T. Ding, L. Yuan, Y. Shen, Q. Zhong, X. Zhang, Y. Cao, B. Hu, T. Zhai, L. Gong, J. Chen, Y. Tong, J. Zhou, Z.L. Wang, *Adv. Energy Mater.* 2 (2012) 1328–1332.
- [11] D. Hanlon, C. Backes, T.M. Higgins, M. Hughes, A. O'Neill, P. King, N. McEvoy, G. S. Duesberg, B. Mendoza Sanchez, H. Pettersson, V. Nicolosi, J.N. Coleman, *Chem. of Mater.* 26 (2014) 1751–1763.
- [12] M.D. Stoller, R.S. Ruoff, *Energy Environ. Sci.* 3 (2010) 1294–1301.
- [13] X. Xiao, T. Li, Z. Peng, H. Jin, Q. Zhong, Q. Hu, B. Yao, Q. Luo, C. Zhang, L. Gong, J. Chen, Y. Gogotsi, J. Zhou, *Nano Energy* 6 (2014) 1–9.
- [14] L. Hu, W. Chen, X. Xie, N. Liu, Y. Yang, H. Wu, Y. Yao, M. Pasta, H.N. Alshareef, Y. Cui, *ACS Nano* 5 (2011) 8904–8913.
- [15] (a) L.Q. Mai, B. Hu, W. Chen, Y.Y. Qi, C.S. Lao, R.S. Yang, Y. Dai, Z.L. Wang, *Adv. Mater.* 19 (2007) 3712–3716;  
(b) Z. Hu, C. Zhou, R. Ramanujam Prabhakar, S. Xiaodai Lim, Y. Wang, J.A. van Kan, H. Cheng, S.G. Mhaisalkar, C.-H. Sow, *J. Appl. Phys.* 113 (2013);  
(c) Z. Hu, C. Zhou, M. Zheng, J. Lu, B. Varghese, H. Cheng, C.-H. Sow, *J. Phys. Chem. C* 116 (2011) 3962–3967;  
(d) X.K. Hu, Y.T. Qian, Z.T. Song, J.R. Huang, R. Cao, J.Q. Xiao, *Chem. Mater.* 20 (2008) 1527–1533;  
(e) C.X. Zhou, Y.X. Wang, L.Q. Yang, J.H. Lin, *Inorg. Chem.* 40 (2001) 1521–1526.
- [16] X. Lu, G. Wang, T. Zhai, M. Yu, J. Gan, Y. Tong, Y. Li, *Nano Lett.* 12 (2012) 1690–1696.
- [17] X. Xiao, Z. Peng, C. Chen, C. Zhang, M. Beidaghi, Z. Yang, N. Wu, Y. Huang, L. Miao, Y. Gogotsi, J. Zhou, *Nano Energy* 9 (2014) 355–363.
- [18] T. Ressler, R.E. Jentoft, J. Wienold, M.M. Günter, O. Timpe, *J. Phys. Chem. B* 104 (2000) 6360–6370.
- [19] (a) X. Xiao, X. Peng, H. Jin, T. Li, C. Zhang, B. Gao, B. Hu, K. Huo, J. Zhou, *Adv. Mater.* 25 (2013) 5091–5097;  
(b) S. Ardizzone, G. Fregonara, S. Trasatti, *Electrochim. Acta* 35 (1990) 263–267.
- [20] (a) M.R. Lukatskaya, O. Mashtalir, C.E. Ren, Y. Dall'Agnese, P. Rozier, P. L. Taberna, M. Naguib, P. Simon, M.W. Barsoum, Y. Gogotsi, *Science* 341 (2013) 1502–1505;  
(b) H. Liu, Z. Bi, X.-G. Sun, R.R. Unocic, M.P. Paranthaman, S. Dai, G.M. Brown, *Adv. Mater.* 23 (2011) 3450–3454;  
(c) M. Zúkalová, M. Kalbáč, L. Kavan, I. Exnar, M. Graetzel, *Chem. Mater.* 17 (2005) 1248–1255.
- [21] M. Heon, S. Lofland, J. Applegate, R. Nolte, E. Cortes, J.D. Hettinger, P.-L. Taberna, P. Simon, P. Huang, M. Brunet, Y. Gogotsi, *Energy Environ. Sci.* 4 (2011) 135–138.
- [22] V. Presser, L. Zhang, J.J. Niu, J. McDonough, C. Perez, H. Fong, Y. Gogotsi, *Adv. Energy Mater.* 1 (2011) 423–430.
- [23] J.K. McDonough, A.I. Frolov, V. Presser, J. Niu, C.H. Miller, T. Ubieta, M. V. Fedorov, Y. Gogotsi, *Carbon* 50 (2012) 3298–3309.
- [24] J.M. Miller, B. Dunn, T.D. Tran, R.W. Pekala, *J. Electrochem. Soc.* 144 (1997) L309–L311.
- [25] (a) P.M. Biesheuvel, *J. Colloid Interface Sci.* 332 (2009) 258–264;  
(b) H. Yin, S. Zhao, J. Wan, H. Tang, L. Chang, L. He, H. Zhao, Y. Gao, Z. Tang, *Adv. Mater.* 25 (2013) 6270–6276;  
(c) J. Benson, I. Kovalenko, S. Boukhalifa, D. Lashmore, M. Sanghadasa, G. Yushin, *Adv. Mater.* 25 (2013) 6625–6632.
- [26] L.S. Aravinda, U. Bhat, B. Ramachandra Bhat, *Electrochim. Acta* 112 (2013) 663–669.
- [27] G.R. Li, Z.L. Wang, F.L. Zheng, Y.N. Ou, Y.X. Tong, *J. Mater. Chem.* 21 (2011) 4217–4221.
- [28] M.F. El-Kady, V. Strong, S. Dubin, R.B. Kaner, *Science* 335 (2012) 1326–1330.
- [29] S. Porada, R. Zhao, A. van der Wal, V. Presser, P.M. Biesheuvel, *Prog. Mater. Sci.* 58 (2013) 1388–1442.